Ore Geology Reviews 120 (2020) 103427

Contents lists available at ScienceDirect

Ore Geology Reviews

journal homepage: www.elsevier.com/locate/oregeorev

Genesis of the telescoped Eocene silver and Oligocene gold San Dimas deposits, Sierra Madre Occidental, Mexico: Constraints from fluid inclusions, oxygen - deuterium and noble gases isotopes

Paula Montoya-Lopera[a], Gilles Levresse[b,*], Luca Ferrari[b], Andrea Luca Rizzo[c], Santiago Urquiza[a], Luis Mata[d]

[a] Posgrado en Ciencias de la Tierra, Universidad Nacional Autónoma de Mexico, Campus Juriquilla, 76230, Queretaro, Qro., Mexico
[b] Centro de Geociencias, Universidad Nacional Autónoma de Mexico, Campus Juriquilla, 76230, Queretaro, Qro., Mexico
[c] Istituto Nazionale di Geofisica e Vulcanologia, Sezione di Palermo, 90146 Palermo, Italy
[d] First Majestic Silver Corp., Tayoltita, Dgo., Mexico

ARTICLE INFO

Keywords:
San Dimas Ag–Au district
Fluid inclusions
D-O stable isotope
Noble gases
Telescoped ore deposits

ABSTRACT

The San Dimas district is a world-class Ag/Au deposit, developed as a telescoped Eocene-Oligocene Ag/Au mineralization located in the Sierra Madre Occidental (SMO) of western Mexico. San Dimas exhibits multiple mineralization events during different magmatic and tectonic episodes from Late Cretaceous to early Oligocene. The well-preserved magmatic-hydrothermal system provides an excellent opportunity to determine the source of silver and gold, the evolution of the hydrothermal fluids, and the controls on the mineralization precipitation. Mineralogical, fluid inclusions (FI), stable and noble gases isotope analyses suggest that the San Dimas deposit consist of two different mineralization styles: 1) Ag-dominant epithermal Eocene veins that occurred at temperatures up to ~350 °C developed at ca. 2–3 km depth, associated to the final stages of intrusion of the Piaxtla batholith, with FI dominated by a crustal component, and 2) epithermal low sulfidation Au-dominant Oligocene veins which were developed at 250 °C, at shallower depths (< 1 km), associated to the feeding fractures of rhyolitic domes developed at the end of the main ignimbrite flare up of the SMO, with FI showing crustal fluids variably mixed with a magmatic component. Our results highlight the importance of a multidisciplinary approach, such as field observations, geochronological and geochemical studies, to better understand the complexity of the hydrothermal magmatic processes involved in the formation of many Mexican ore deposits and their proper classification.

1. Introduction

Since the early 20th century, economic geologists have recognized epithermal deposits as being important sources of silver and gold (Lindgren, 1922). More than 6000 tons of gold (Au) resources have been proven from worldwide epithermal systems and keep growing (Kerrich et al., 2000; Chen et al., 2003, 2012; Zhang et al., 2019). In the still valid original description of Lindgren (1922, 1933), an epithermal deposit is usually defined as the "sub-aerial volcanic-hosted types". The typical characteristics of this kind of deposits are a structurally controlled extensional vein system, geographically and chronologically associated to a volcanic center (usually rhyolite domes) that formed in a shallow environment (< 1 km below the water table) and involving predominantly near neutral chloride waters (mostly of meteoric origin) at relative low temperatures (typically 150–300 °C) and low sulfidation (LS) mineralogy (Heald at al., 1987; Panteleyev, 1996; White, 2003; Pirajno, 2009). Later, Heald et al., (1987), Hedenquist (1987), and Simmons et al., (2005) among many others, described comparable mineralized structure related to deeper porphyries mineralization environments. These are characterized by acidic magmatic fluids (high temperature and salinity), deeper metals precipitation, gangue and alteration mineralogy (alunite, dickite, kaolinite) and related to high sulphidation (HS) state. These well-defined genetic models can be seen as two pure end-members of a common family, since many epithermal-like deposits do not fit in them. To solve this problem, John (1999), John et al., (1999) and Hedenquist and Arribas (2000) proposed a third epithermal class named intermediate-sulfidation (IS) type to explain and regroup the large variety of the structurally controlled deposits,

* Corresponding author.
E-mail address: glevresse@geociencias.unam.mx (G. Levresse).

https://doi.org/10.1016/j.oregeorev.2020.103427
Received 30 October 2019; Received in revised form 12 February 2020; Accepted 18 February 2020
Available online 21 February 2020
0169-1368/

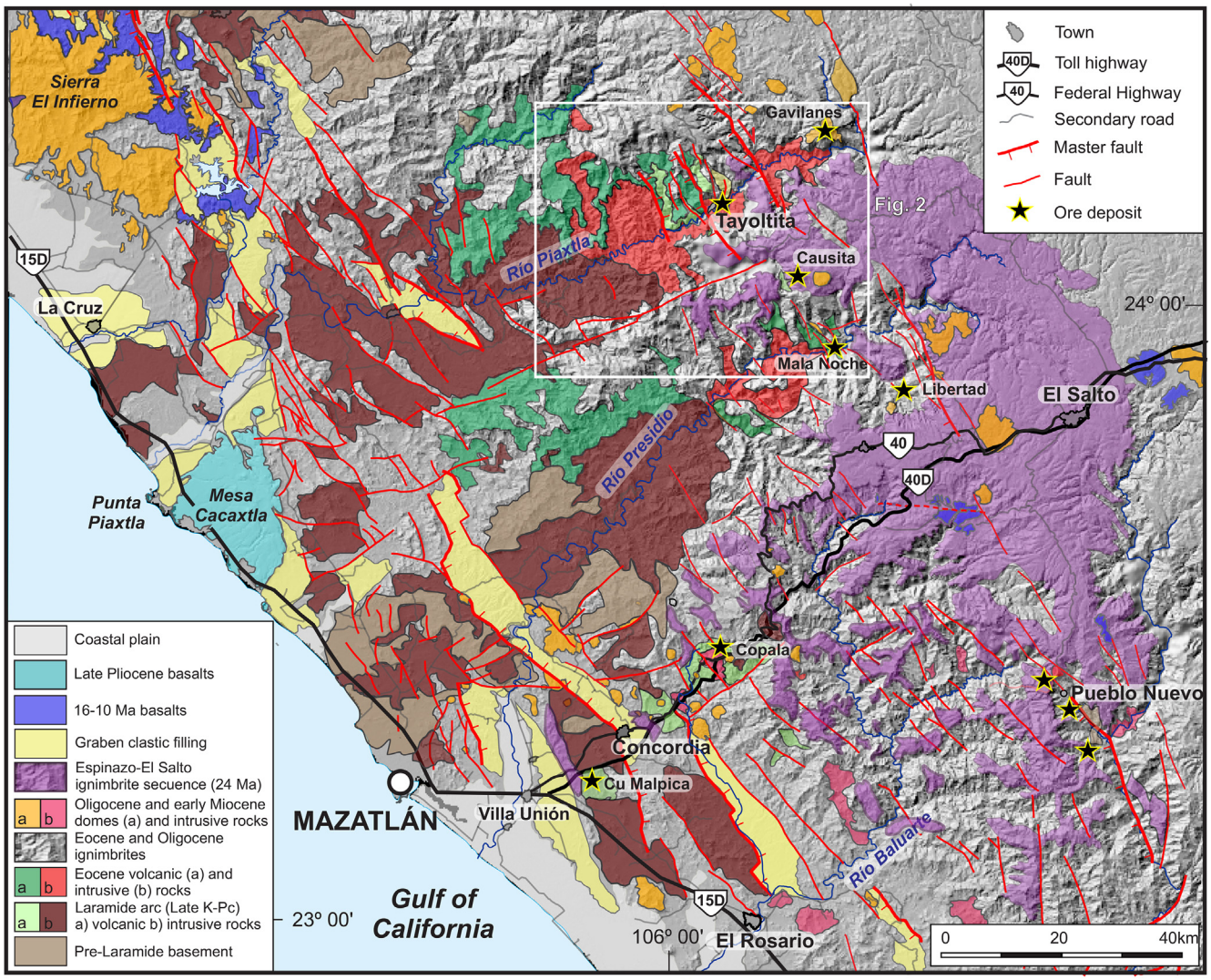

Fig. 1. Regional geologic map of central Sierra Madre Occidental showing the main post-Eocene extensional structures and the principal mining districts (modified from Henry and Fredrikson, 1987, and Ferrari et al., 2013). Insert show the spatial distribution of the Sierra Madre Occidental (SMOc) volcanic province and the San dimas district (SDD) location.

from Cordilleran polymetallic to carbonate-base metal Au deposits (Einaudi, 1992; Leach and Corbett, 1994; Wang et al., 2019 and references therein).

In Mexico, a review of epithermal deposit classification, including the classic San Dimas Au/Ag district, was proposed by Camprubi and Albinson (2007). The size of the Mexican silver and gold anomaly is illustrated by the outstanding play of Mexico mining during XVI and XVII centuries and its last ten years position as the largest silver (200 Moz/year) and eighth gold producer (125 t/year) worldwide. Most of this production comes from localities within the Sierra Madre Occidental province (SMO) and the magmatic events related to its formation. The chronological distribution of epithermal deposits coincides with the three main Cenozoic volcanic pulses of the SMO, which record a broad migration from the northwest to the southeast, where the last ignimbrite flare-up occurred (Ferrari et al., 2007, 2018; Ramos-Rosique et al., 2010; Fig. 1). The age of the most fertile events ranges from 36 to 28 Ma and includes all the giant Ag–Au–Sn and IOCG mining districts (Camprubí, 2013). Few epithermal deposits in México are known to have formed under an acid chemical regime. In fact, HS deposits were only recognized in Sonora state, in close relationship to the Cu-porphyry province (Camprubí, 2013). The recent re-evaluation of various historical Au/Ag districts (Guanajuato, Moncada et al., 2012, 2017; Fresnillo, Velador, 2010; Zacatecas, Zamora-Vega et al., 2018; San Dimas, Montoya et al., 2019b) is modifying several crucial concepts about timing, formation, and metals sources of the dominant intermediate and low sulfidation Mexican epithermal deposits. Some of them, traditionally classified as intermediate sulfidation, are now reinterpreted as telescoped deposits, formed during separate volcanic events sometimes under different geodynamic contexts (Zamora-Vega et al., 2019; Montoya-Lopera et al., 2019b).

In this study, we report on the description and geochemistry of fluid inclusions (FI) hosted in the Eocene silver-dominant and Oligocene gold-dominant mineralizing deposits found in the San Dimas district (Fig. 1). Building on recent geological, geochronological and geochemical studies (Montoya et al., 2019a; Montoya-Lopera et al., 2019b), we describe the TPX evolution of the ore-forming fluids and the ore genesis, to finally propose a new metallogenic model for the San Dimas Ag/Au deposit.

2. San Dimas local geology and mineralization settings

The San Dimas stratigraphic column can be divided into two major igneous successions that correspond to the Lower Volcanic Complex (LVC) and Upper Volcanic Supergroup (UVS) of the SMO, separated by

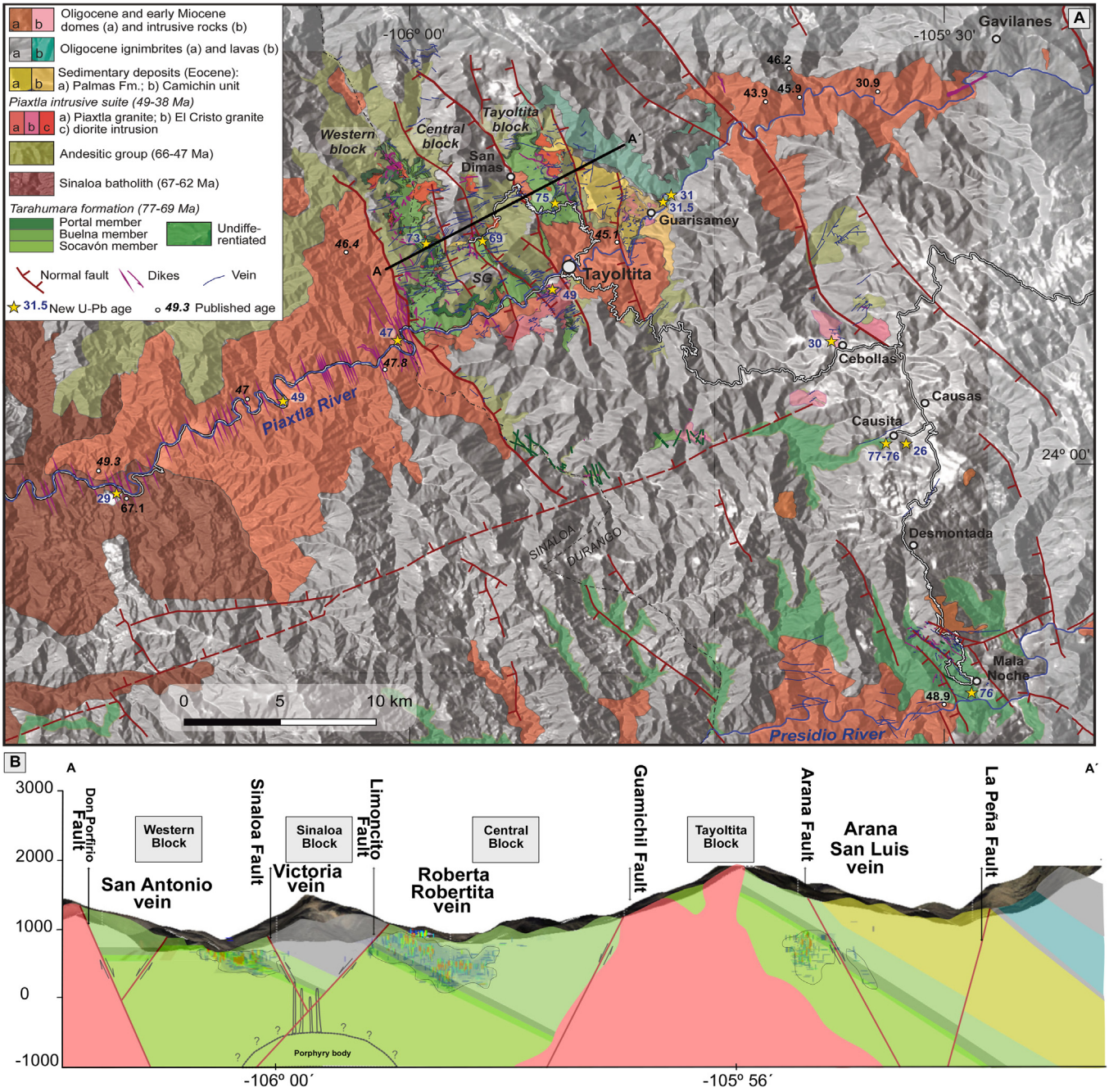

Fig. 2. (A) Geologic map of San Dimas mining district and Causita and Mala Noche southern extension, with location of published ages (from Montoya et al., 2019a) and sampled veins. (B) Simplified geological cross-section of the Ag/Au San Dimas district.

erosional and depositional unconformities. A detailed description of the lithology, petrography and geochronology of the stratigraphic column is given in Montoya et al., (2019a) and is briefly summarized here.

The Late Cretaceous to Eocene LVC, is composed of four volcanic members locally named "Socavón rhyolite", "Buelna andesite", "Portal rhyolite" and the Andesitic Group (Henshaw, 1953; Montoya et al., 2019a; Fig. 2). The LVC consists of an alternating suite of rhyolitic and andesite lavas flows locally intruded by felsic porphyritic bodies (Montoya et al., 2019a). The entire LVC volcanic column is crosscut and locally assimilated by the late Eocene Piaxtla batholith and its porphyritic dikes swarm (49.1–45.2 Ma; Henry et al., 2003; Montoya et al., 2019a). The transition between the LVC and the UVS is marked by the Las Palmas and Camichin continental sedimentary formations with a maximum age of deposition of ~52 Ma and ~43 Ma, respectively (Montoya et al., 2019a). The UVC unconformably covers the La Palmas and Camichin formations, the Piaxtla batholith and the Andesite Group. It is composed by two successions of silicic ignimbrites with ages of ~31.5 to 29 Ma and ~24 Ma respectively, with intercalations of minor amount of mafic lavas and continental conglomerate (Montoya et al., 2019a). The lower ignimbrite succession is intruded by rhyolitic domes dated at ~29 Ma and bimodal dikes swarm (Ferrari et al., 2013; Montoya et al., 2019a).

The San Dimas district is affected by two main fault systems with E-W and NNW-SSE orientation. Both systems present various reactivation events and are mineralized (Horner and Enriquez, 1999; Enriquez et al., 2018; Montoya et al., 2019a). The E-W fault system affects mainly the LVC and is overprinted by the NNW-SSE one. The main NNW-SSE striking normal faults divide the district in tilted fault blocks, dipping

up to 30° to the east or to the west. Based on veins paragenesis sequence and $^{40}Ar/^{39}Ar$ ages, Montoya et al. (2019b) propose that mineralization occurs in two discrete hydrothermal events, a first Eocene Ag-dominant vein system (adularia + rhodochrosite type; ca. 41–40 Ma), mainly developed into E-W striking faults, followed by a Au-dominant epithermal vein mineralization (sericite type; ca. 30 Ma), which was emplaced into NNW-SSE striking faults concurrent with Oligocene rhyolitic domes related to the final stage of the first SMO ignimbrite flare up.

3. Previous fluid inclusions studies of the San Dimas Ag–Au district

Previous hydrothermal fluid studies at San Dimas mainly focused on the "bonanza" level Au-dominant structures of the Tayoltita Block (Fig. 2). Homogenization temperatures for quartz Au/Ag-mineralizing stage range from 250 °C to 310 °C, averaging 260 °C in all studies (Smith et al., 1982; Clarke and Title, 1988; Conrad et al., 1992; Enriquez and Rivera, 2001; Albinson et al., 2001; Churchill, 1980). Reported freezing point show a tide variation range from −0.11 °C to −1.5 °C. (Smith et al., 1982; Clarke and Title, 1988; Conrad et al., 1992; Enriquez and Rivera, 2001). Smith et al., (1982) report positive last solid fusion temperatures ranging from 0.3 °C to 2.9 °C, suggesting clathrate fusion and occurrence of CO_2. They also describe heterogeneous trapping and vapor and liquid phase homogenization processes, suggesting occurrence of boiling. Clark and Titley (1988), present a reverse correlation between Ag/Au ratio and FI salinity. FI data and field relationships indicate an approximate 400 to 1000 m depth range below the surface for the bonanza level at the time of vein formation (Smith et al., 1982; Clark and Titley, 1988). The $\delta^{18}O_{qtz}$ values of Au/Ag mineralizing quartz event range from 3.9 to 9.5‰. Recalculated $\delta^{18}O_{H2O}$ range from −2.9 to 3.7‰, indicating that meteoric water dominated the hydrothermal system (Smith et al., 1982; Conrad and Chamberlain, 1992). Gas spectrometry indicates that water constituted over 99.5 mol percent of the liquid and gas phases, with CO_2 comprising most of the remaining gases, minor CO and traces of H_2, CH_4, N_2, C_2H_6, H_2S, C_3H_8, SO_2 and NO (Smith et al., 1982).

4. Results

Analytical techniques and detailed data are presented in supplementary files.

4.1. Decriptometry

Fig. 3 presents the results of the decrepitation experiment of twenty quartz populations from nine Au- and Ag-dominant veins representative of the San Dimas district as well as its southern extension. All samples display a more or less defined bimodal distribution pattern. The two maximum peaks range from 200 to 220 °C and 400 to 440 °C (Fig. 3A). In a few samples a third high temperature peak roughly developed above 550 °C (Fig. 3A). Burlinson et al. (1983, Burlinson et al., 1988) suggest that peaks like these are not related to FI decrepitation but to quartz crystallization phase transition, therefore should not be considered. Quartz cements from the "Bonanza" level are characterized by higher FI decrepitation count per 10 s than samples collected at the top or at the root of the veins.

Plotting the 400 °C/200 °C peak intensity ratios versus Au/Ag ratio allows distinguishing both Ag- and Au-dominant hydrothermal events (Fig. 3B). The plot also shows a positive relationship between the 200 °C peak intensity with Ag concentration (Fig. 3B).

4.2. Vein and fluid inclusions petrography and microthermometry

The Ag- and Au-dominant veins paragenetic sequence is detailed in Montoya et al. (2019b) and presented in Fig. 4. Ag-dominant veins are characterized by three stages of formation named open, filling and close stage. The opening stage shows open space filling quartz texture. The filling stage corresponds to the mineralization and is characterized by mosaic quartz texture. The closing stage present crack-seal and open space filling quartz texture (Fig. 4).

Based on the petrographic and compositional features of the FI at room temperature, two types were identified: type I and type II. Type I is the dominant type recognized in both Ag- and Au-dominant events and corresponds to two phases liquid–vapor (LVaq), liquid dominant inclusions, with estimated vapor volume of 5 to 10%. Type I primary FI (LVaq) are either found as isolated inclusions, in small clusters, or in quartz growing plans. This population of FI yields very homogeneous volume ratios (Fig. 4 A,B, C). Typically, the FI are negative crystals to ovoid in shape and are less than 20 μm in length. Type II is recognized principally in the filling stage of the Ag-dominant event and corresponds to two-phases vapor dominant (VLaq) inclusions, with estimated vapor volume up to 90% (Fig. 4 D, E, E). Type II FI (VLaq) are crystal negative to ovoid in shape and are less than 30 μm in length. The visual estimate of the liquid-to-vapor ratio is highly variable. These FI are only found in small clusters.

The opening stage presents the highest homogenization temperature. The type I fluid inclusion homogenize to liquid between 128 °C and 320 °C, with a poorly defined modal distribution (median at ca. 240 °C; Fig. 5 A, B; table 1). Final ice melting temperatures occurs between −0.9 °C and 0.3 °C, corresponding to 0 and 1.57 wt% NaCl eq (Fig. 5 C).

The filling stage presents two biphasic fluid inclusions types, liquid dominant (LVaq) and vapor dominant (VLaq). Final homogenization temperatures range from 122 °C to 304 °C with a well-defined unimodal distribution and a median value at ca. 140 °C (Fig. 5A, B). Final solid melting temperatures present a wider distribution, including ice and clathrate melting at temperatures varying from −0.5 °C to 5.6 °C, corresponding to 0 and 0.88 wt% NaCl eq (Fig. 5C).

In the closing stage, type II (LVaq) fluid inclusions homogenize to liquid from 120 °C to 318 °C with a bimodal statistical distribution, with maximum values at 140 °C and 230 °C. Final ice melting temperatures are almost constant, varying between −1.9 °C and 0.0 °C corresponding to 0 and 3.22 wt% NaCl eq (Fig. 5C).

In the Au-dominant veins, the biphasic LVaq FI in the quartz stage yield final ice melting temperatures ranging from −1.4 °C to −0.0 °C, corresponding 0 and 2.4 wt% NaCl eq. Total homogenization occurs in the liquid phases at temperatures ranging from 121 °C to 316 °C in a bimodal distribution (Fig. 5B, D and Table 1).

On a diagram of last melting temperature (Tm) versus homogenization temperature (Th) (Fig. 5C, D), the Ag- and Au-dominant FI from San Dimas district veins swarm overlap historic data trend compilations (Smith, 1982; Conrad et al., 1992; Enriquez and Rivera, 2001). Both Ag- and Au-dominant events record the same evolution from high to low homogenization temperatures with low salinity values, suggesting an adiabatic cooling process in a dominant meteoric environment (Fig. 5C, D). The Ag-dominant filling stage presents low homogenization and positive fusion temperatures indicating clathrate fusion and the presence of dissolved CO_2.

Micro-infrared spectrometry analysis was performed to show the CO_2 concentration in the different events/stages of Au/Ag mineralization. In all Ag- and Au-dominant events analyzed samples, CO_2 concentration in FI vapor phase remain within the analytical noise, including in LVaq vapor dominant inclusions. However, CO_2 concentration was detected in water liquid phase in analyzed fluid inclusions from both mineralization events. CO_2 concentration increases notably in the Ag-dominant filling stage event.

4.3. Fluid inclusions $\delta^{18}O$ and δD isotope analysis

$\delta^{18}O$ and δD isotopic data are presented in Table 2 and Fig. 6 in ‰ deviation relative to the SMOW standard. Data are grouped according to mineralized stages from the older to the more recent. From Victoria

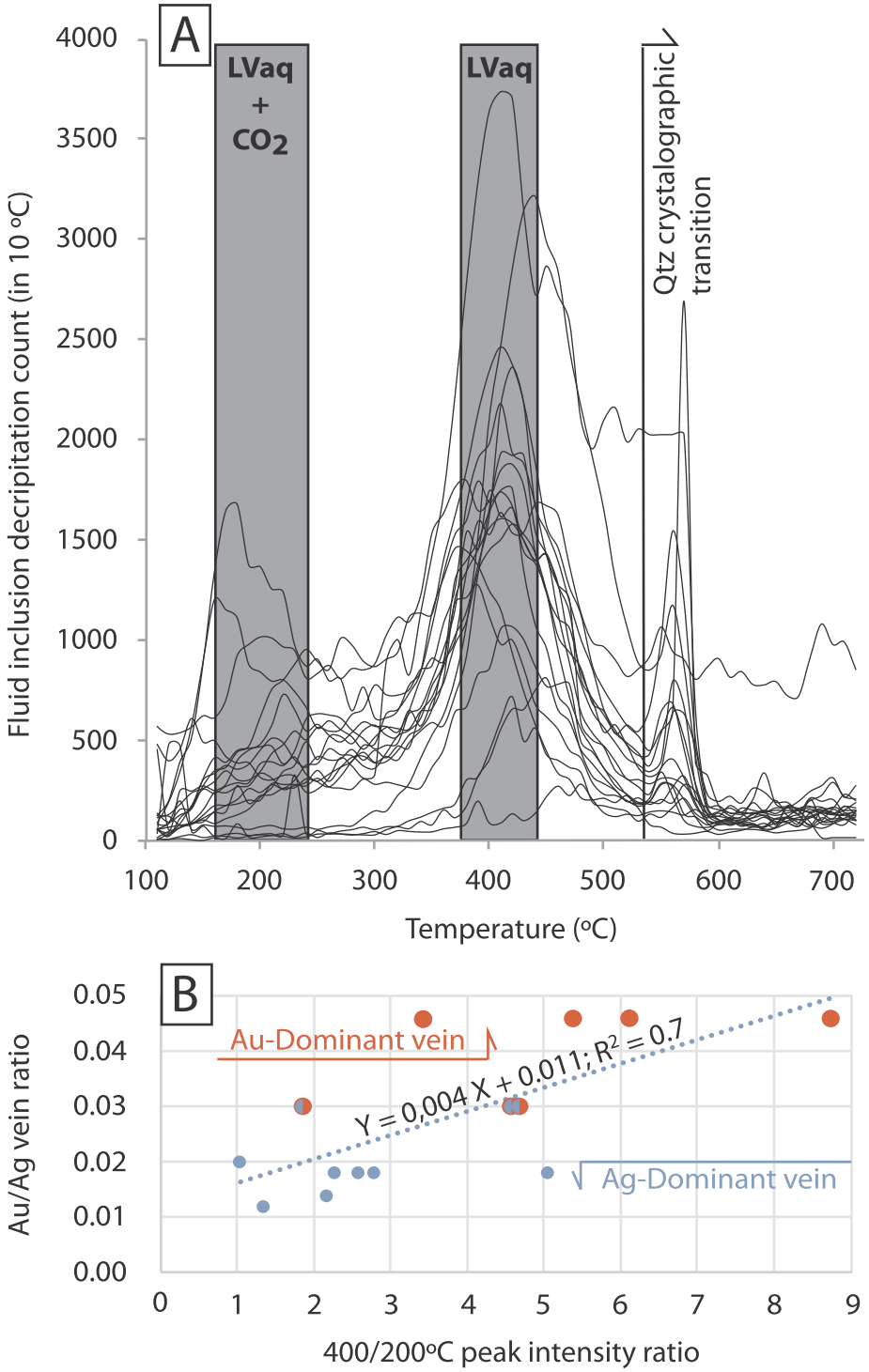

Fig. 3. (A) FI decrepitation diagram of Ag-dominant and Au-dominant quartz veins from Ag/Au San Dimas district. (B) 400/200 °C peak intensity ratio versus Au/Ag metals ratio sample diagram of Ag-dominant and Au-dominant quartz veins from the Ag/Au San Dimas district.

and Robertas Eocene Ag-dominant veins, we analyze six FI populations from opening (n = 1), filling (n = 4) and closing (n = 1) quartz cement stages. The analyzed δD values display a narrow range from −87.98‰ to −63.02‰ whereas the measured $\delta^{18}O$ values display a relatively large range, from −8.79‰ to 10.34‰ (Table 2). $\delta^{18}O$-δD fluid inclusions isotopic signature of Robertas quartz filling stage was detailed following its thermal decrepitation pattern (Fig. 6). Fluid inclusions population in the range 110 °C − 310 °C shows $\delta^{18}O$-δD isotopic signature of 10.34‰ and −87.98‰, whereas that in the 310 °C to 550 °C range has $\delta^{18}O$-δD signature of −0.54‰ and −88‰. Once plotted in the $\delta^{18}O$-δD diagram the results are distributed along a mixing line from the global meteoric water line (GMWL) to the primary magmatic water field. The opening and closing stages results plot closer to the GMWL than the filling (mineralizing) stage, which plot toward or within the Mexican active geothermal fields and epithermal deposits fields.

Four samples from four different Au-dominant veins were analyzed (Arana vein, Causita vein, San Luis vein and San Antonio vein; Fig. 6; table 2). The $\delta^{18}O$-δD values range from −5.13‰ to 1.61‰ and from −72.20‰ to −45.81‰. In the $\delta^{18}O$-δD diagram the results obtained

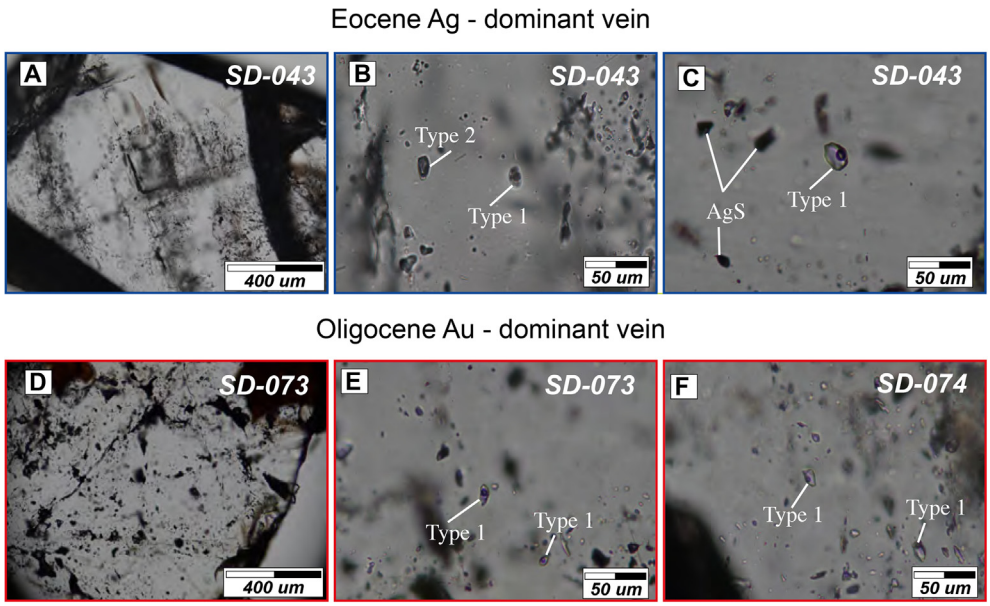

Fig. 4. Photomicrographs image of fluid inclusions paragenesis. (A) Filling quartz stage (mineralization stage) from Roberta vein with primary FI trails along growing quartz plans; (B) Type 1 and type 2 association; Type 2-Primary biphasic Liquid-dominant FI; Type 2-Primary biphasic gas-dominant FI; (C) Type 1-Primary biphasic Liquid-dominant FI associate with silver droplets; (D); Sulphide mineralizing quartz from San Antonio vein with primary biphasic Liquid-dominant FI clouds; (E) Type 1-Primary biphasic Liquid-dominant FI; (F) Type 1-Primary biphasic Liquid-dominant FI.

from Arana, Causita, San Luis and San Antonio Au-dominant veins overlap the Ag-dominant mineralized filling stage isotopic trend data and plot between the LS and IS Mexican epithermal deposit and active geothermal fields.

4.4. Chemistry and noble gas isotope composition of fluid inclusions

4.4.1. Chemistry

For the Eocene Ag-dominant veins we analyzed quartz samples from

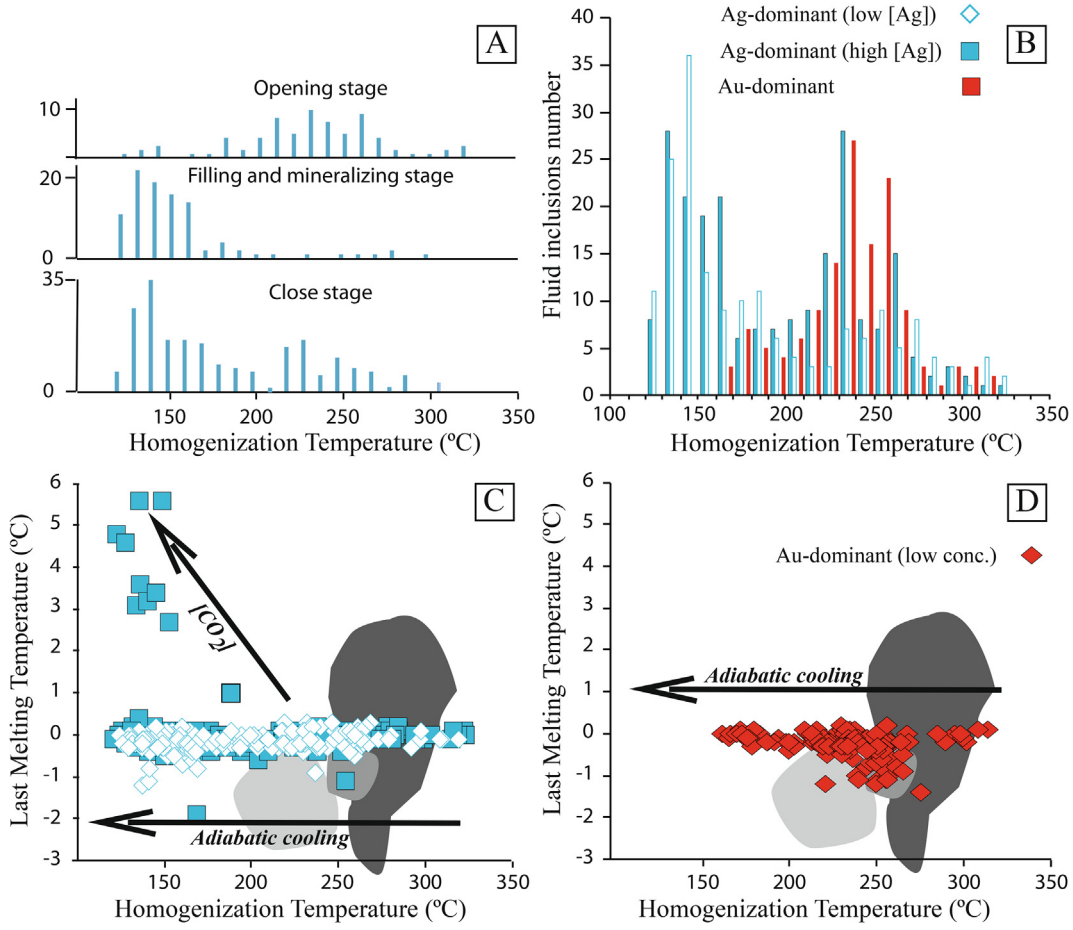

Fig. 5. (A) Homogenization temperature histograms for FI from Ag-dominant opening, filling and close stages. (B) Homogenization temperature histograms for FI from Ag-dominant and Au-dominant quartz events. (C) Homogenization temperature and ice melting temperature plot for Ag-dominant quartz gangue. (D) Homogenization temperature and ice melting temperature plot for Au-dominant quartz gangue. Dark grey area: FI from Smith et al., (1982); grey area: FI from Clark and Titley (1988); light grey area: FI from Enriquez and Rivera (2001a).

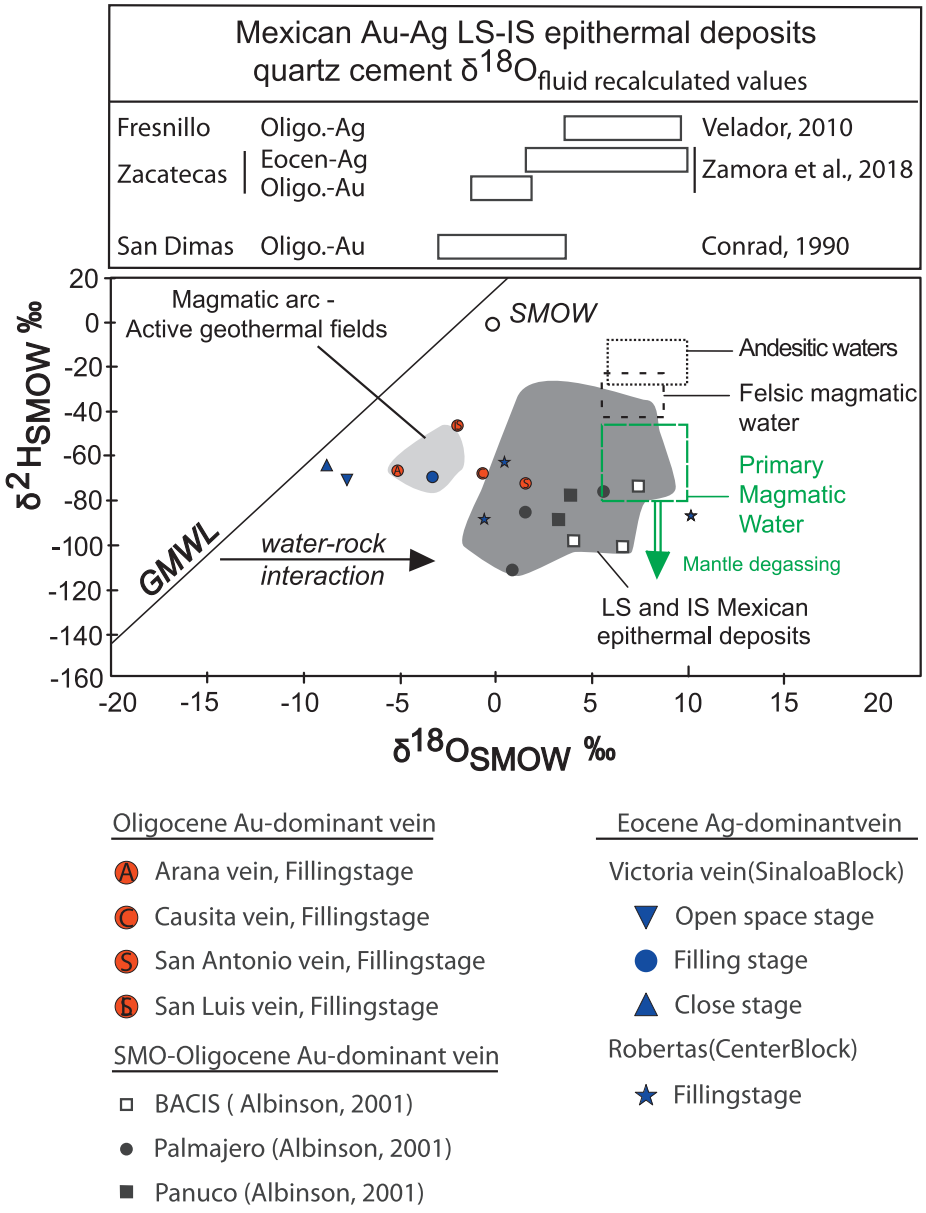

Fig. 6. $\delta^{18}O$-δD diagram of the Eocene Ag-dominant and Oligocene Au-dominant mineralized veins from the San Dimas Au/Ag district. The epithermal deposit field is drawn from Albinson et al. (2001), Camprubi. (2013), Velador, (2010); Simmons et al. (1986); and Zamora Vega et al. (2018). Primary magmatic water, felsic water and Andesitic water fields are taken from Sheppard et al., (1969), Taylor, (1974), Sheppard, (1986), and Giggenbach, (1992a and 1992b). Mexican active geothermal sites: Los Azufres and Los Humeros related to magmatic arc are taken from Pinti et al. (2013) and references therein.

the open-filling and closing stages of the Victoria vein and for the filling stage of the Roberta vein. Quartz samples for the Oligocene Au-dominant vein come from the filling stage of the Arana, San Antonio, San Luis, Causitas and Mala Noche veins (Figs. 7 and 8). The chemistry of FI and noble gases isotopic ratio is given in Table 3. Measurement uncertainties for some samples are relatively high because the amount of gas extracted from these samples was small.

H_2O is the dominant species of FI and varies between $3.6{\cdot}10^{-6}$ and $3.0{\cdot}10^{-5}$ mol g^{-1} (average $1.4{\cdot}10^{-5}$ mol g^{-1}) in the Eocene Ag-dominant vein, and between $4.4{\cdot}10^{-6}$ and $2.5{\cdot}10^{-5}$ mol g^{-1} (average $1.3{\cdot}10^{-5}$ mol g^{-1}) in the Oligocene Au-dominant vein. CO_2 and N_2 are the other major components of FI. CO_2 ranges between $7.1{\cdot}10^{-9}$ and $2.5{\cdot}10^{-8}$ mol g^{-1} (average $1.6{\cdot}10^{-8}$ mol g^{-1}) in the Eocene Ag-dominant vein, and between $8.2{\cdot}10^{-9}$ and $1.8{\cdot}10^{-7}$ mol g^{-1} (average $4.8{\cdot}10^{-8}$ mol g^{-1}) in the Oligocene Au-dominant vein. N_2 varies in a narrow range between $3.1{\cdot}10^{-8}$ and $4.1{\cdot}10^{-8}$ mol g^{-1} (average $3.7{\cdot}10^{-8}$ mol g^{-1}) in the Eocene Ag-dominant vein, while between $1.6{\cdot}10^{-8}$ and $7.1{\cdot}10^{-8}$ mol g^{-1} (average $3.7{\cdot}10^{-8}$ mol g^{-1}) in the Oligocene Au-dominant vein (Fig. 7; Table 3).

Helium varies from $8.7{\cdot}10^{-14}$ to $9.2{\cdot}10^{-13}$ mol g^{-1} (average $3.0{\cdot}10^{-13}$ mol g^{-1}) in the Eocene Ag-dominant vein, while between $3.3{\cdot}10^{-14}$ and $8.1{\cdot}10^{-13}$ mol g^{-1} (average $2.8{\cdot}10^{-13}$ mol g^{-1}) in the Oligocene Au-dominant vein. Helium corrected for atmospheric contamination ($^4He_{corr}$) shows comparable range of values (mean values within 10%), except for the most air contaminated samples. ^{20}Ne varies from $4.4{\cdot}10^{-14}$ to $7.6{\cdot}10^{-14}$ mol g^{-1} (average $5.6{\cdot}10^{-14}$ mol g^{-1}) in the Eocene Ag-dominant vein, while between $3.7{\cdot}10^{-14}$ and $1.1{\cdot}10^{-13}$ mol g^{-1} (average $6.8{\cdot}10^{-14}$ mol g^{-1}) in the Oligocene Au-dominant vein. ^{40}Ar varies in a narrow range from $1.8{\cdot}10^{-11}$ to $2.6{\cdot}10^{-11}$ mol g^{-1} (average $2.1{\cdot}10^{-11}$ mol g^{-1}) in the Eocene Ag-dominant vein, while between $1.3{\cdot}10^{-11}$ and $3.5{\cdot}10^{-11}$ mol g^{-1} (average $2.2{\cdot}10^{-11}$ mol g^{-1}) in the Oligocene Au-dominant vein.

In terms of chemistry, we do not notice appreciable differences between the Eocene Ag- and the Oligocene Au-dominant veins, with a

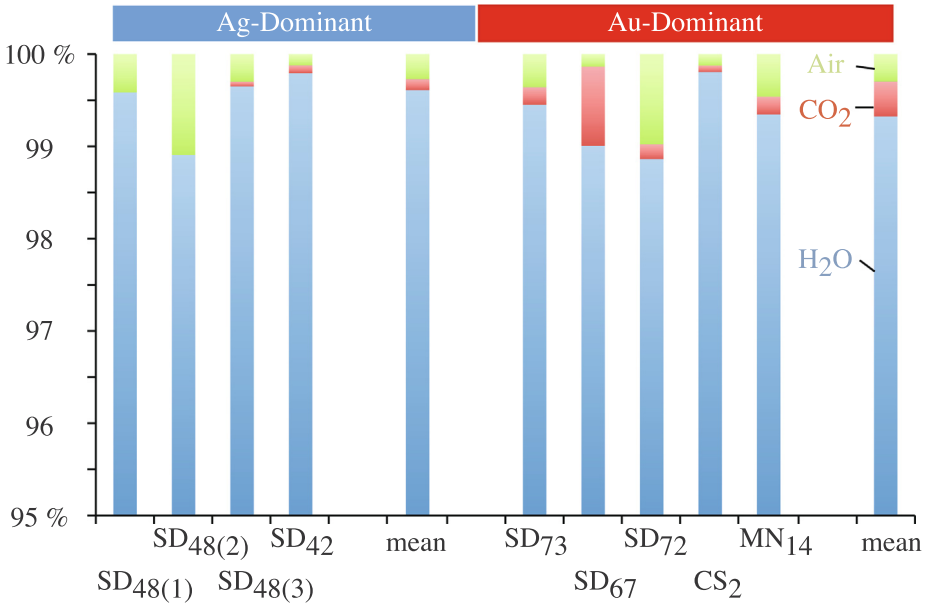

Fig. 7. Major and noble gases Eocene and Oligocene fluid inclusions composition.

general overlap between the two groups of samples.

4.4.2. Noble gas isotope composition

The Eocene and Oligocene quartz $^{4}He/^{20}Ne$ ratios vary from 1.2 to 20.7 and from 0.4 to 11.7, respectively, indicating a strong contribution from an atmospheric-derived component (Ozima and Podosek, 2002). $^{40}Ar/^{36}Ar$ ratios vary from 295.13 to 304.04 (average 298.99) and from 294.04 to 319.71 (average 300.66), respectively, supporting the indications from $^{4}He/^{20}Ne$ (Ozima and Podosek, 2002). $^{20}Ne/^{22}Ne$ and $^{21}Ne/^{22}Ne$ ratios from Eocene and Oligocene quartz give similar indications: 9.79 to 9.81 and 0.0285 to 0.0291, respectively. Fig. 8A is a plot of $^{21}Ne/^{22}Ne$ versus $^{20}Ne/^{22}Ne$ showing trajectories for radiogenic and nucleogenic Ne production extending outward from the air value. Within the error margin all samples plot near the air value. Some Oligocene Au-dominant results plot slightly below it, suggesting a small influence of degassing processes consistent with a hydrothermal component in the gas (Ballentine, 1997, and references therein). Fig. 8B plots Argon (mol/g) versus neon (mol/g) showing air and air saturated water line distribution (Ozima and Podosek, 2002). Within the error margin all samples plot near the air-line.

The $^{3}He/^{4}He$ ratios not corrected for atmospheric contamination (R/Ra) from Eocene Ag-dominant (0.08–0.24 Ra, mean 0.19 Ra) are on average lower than for the Oligocene Au-dominant (0.07–1.19 Ra, mean 0.57 Ra), with a partial overlapping of values from both deposits (Fig. 8C). He corrected for air contamination ($^{4}He_{corr}$) versus Rc/Ra plot (Fig. 8C) shows that overall the two events are in partial overlapping. Au-dominant Oligocene samples are well distributed along a crust-magmatic mixing line, pointing out the predominance of crustal fluids and variable contributions of a "hypothetical local magmatic" reservoir at about 3 Ra. Ag-dominant Eocene samples present a lateral shift, suggesting a dominant presence of crustal fluids. In the $^{4}He/^{40}Ar$ versus R/Ra plot (Fig. 8D) we get similar information, confirming our previous inference of air-crust mixing for most of the samples, except Causita, San Antonio, and Arana samples from Oligocene Au-dominant veins suggesting He_{mantle} contribution in a 3-component mixing. Considering $^{3}He/^{4}He$ ratio values of 0.01–0.05 Ra for the crust and 8 Ra for a MORB-like mantle ($R/Ra = 8 \pm 1$; Graham, 2002), the He_{mantle} contribution is estimated to be up to 1.7% and 24% in the Ag- and Au-dominant veins samples, respectively.

Accordingly, the $^{3}He/^{4}He$ ratios corrected for atmospheric contamination (Rc/Ra) from Eocene Ag-dominant samples (0.07–0.13 Ra, mean 0.10 Ra) is lower than for the Oligocene Au-dominant samples (0.05–1.91 Ra, mean 0.81 Ra), with a partial overlapping of values from both deposits.

5. Discussion

5.1. Sources and evolution of Eocene Ag- and Oligocene Au-dominant ore-forming fluids

The origin of the ore-forming fluids cannot effectively constrain the source of the ore-forming metals. However, they illustrate well the dynamic of the hydrothermal system, metals transport and precipitation conditions. Petrographic examination of FI assemblages provides evidence concerning the chemical and physical conditions of formation of hydrothermal deposits (Bodnar et al., 1985). Two FI assemblages and compositional features were identified in both the Eocene and Oligocene hydrothermal structures: 1) Type I, two phase liquid–vapor (LVaq), liquid dominant, with estimated vapor volume percent of 5 to 10, is the main dominant type recognized in both events; 2) Type II, two-phase vapor dominant (VLaq), with estimated vapor volume percent up to 90, is recognized principally in the filling stage of the Ag-dominant event in the highest Ag grade mineralized area. The presence of vapor-dominated inclusions, the heterogeneous liquid/vapor ratios and the hockey stick shape distributions in the Th vs Tm diagram suggest that boiling was an important process during silver precipitation. The chemistry of FI confirms that H_2O is the major component. In addition, the lack of clear differences in salinity between the Eocene and Oligocene hydrothermal events confirms that Type I FI dominates within the two events and that Type II FI poorly or not contributed to the extracted gas mixture (Fig. 7).

Fluid inclusions microthermometry and FTIR spectroscopy indicate that ore-forming fluid belongs to the H_2O-NaCl-(CO_2) system and has high to low temperature (ca. 320–120 °C) and low salinity. Eocene and Oligocene hydrothermal events homogenization temperature and salinity data are comparable to those described in the literature (Smith, 1982; Conrad et al., 1992; Enriquez and Rivera, 2001). The overlapping of their homogenization temperature ranges prevents using the microthermometry technique to discriminate both events. However, the Eocene Ag-dominant hydrothermal event is characterized by positive ice melting temperature. The low salinity of the solutions, the small amounts of dissolved CO_2 content, and the absence of trapped minerals

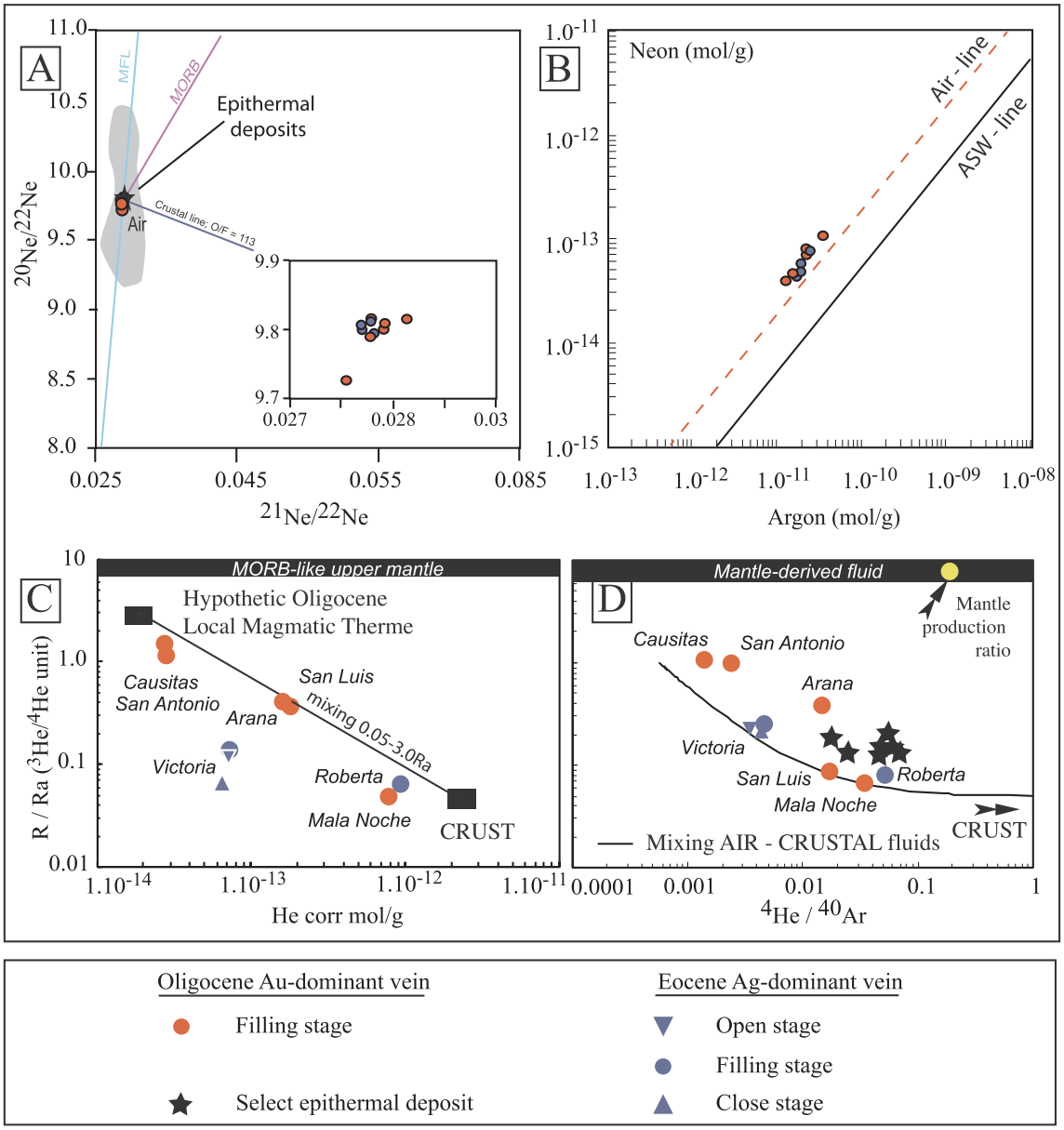

Fig. 8. Noble gases and helium isotope geochemistry diagrams. (A) $^{20}Ne/^{22}Ne$ vs. $^{21}Ne/^{22}Ne$ plot of the Eocene and Oligocene fluid inclusions. The MORB line represents mixing between atmospheric neon and that measured in the upper mantle (Sarda et al., 1988). The crust line represents the evolution of neon isotopic composition by nucleogenic production of ^{20}Ne, ^{21}Ne, $^{22}Ne^*$ in a crustal source having constant O/F ratio of 113 (Kennedy et al., 1990). MFL is the mass fractionation line depicting the isotopic variations of Ne produced by a diffusion-controlled degassing process. (B) Plot of Argon (mol/g) versus Neon (mol/g) including the air- and ASW-line distribution. (C) Plot of R/Ra versus $^{4}He/^{20}Ne$, with mixing trend fitting the data. (D) Plot of R/Ra versus $^{4}He/^{40}Ar$, with air and crustal fluid mixing trend. The assumed mantle and crustal production ratios are taken from Marty (2012) and Ballentine et al. (1994, 2002), respectively. Black stars are compiled data from worldwide mesothermal granite related deposits (references in table).

(halite, sylvite) suggest that the main component is meteoric water. These evidences are corroborated by the chemistry of FI, which clearly indicates H_2O as the major component and significantly low to absent CO_2 content (Fig. 7). In the Eocene and Oligocene hydrothermal events, the FI microthermometric results reveal a continuous adiabatic cooling of the fluid and an increase of CO_2 content during the Ag-dominant filling stage.

$\delta^{18}O$-δD are considered to provide precise information about the sources and evolution of ore-forming fluids (Taylor, 1974). Plotted in the $\delta^{18}O$-δD diagram, both Eocene and Oligocene mineralizing FI are distributed along a mixing line from the global meteoric water line (GMWL) to the primary magmatic water field (Fig. 6). During the Eocene Ag-dominant hydrothermal system, the opening and closing stages data are close to the GMWL, showing the dominance of meteoric fluids, whereas the filling (mineralizing) stage results plot in or near the Mexican active geothermal fields. The $\delta^{18}O$ shift to less negative values of these samples suggests a magmatic input in the mixing fluids isotopic equation. The $\delta^{18}O$-δD data of the Au-dominant hydrothermal events are similar to those of numerous SMO and Mexican LS and IS epithermal deposits (Fig. 6). The $\delta^{18}O$-δD data of the Au-dominant hydrothermal event show a range of compositions indicating that ore fluids are partially magmatic-derived. The obtained $\delta^{18}O$ values suggest mixing and the involvement of meteoric water into the ore fluid, which could lead to the lower $\delta^{18}O$ values. This is also consistent with the measured low homogenization temperatures and salinities of fluids in the Au-dominant event.

The He-Ar-Ne abundance and isotope ratios are a powerful tool in discriminating meteoric, magmatic and crustal reservoirs of the

different fluids (Ballentine, 1997; Ozima and Podosek, 2002). Ar and Ne isotopic data as well as $^4He/^{20}Ne$ and $^4He/^{40}Ar$ ratios indicate that Ar and Ne in both Eocene and Oligocene FI samples are mainly atmospheric (table 3; Fig. 8C and 8D), with very minor nucleogenic production from halogens (F) and crustal contamination (K). The conservative behavior of helium and the difference in isotopic composition between the crust ($^3He/^4He$ = 0.01–0.05 Ra; Ballentine et al., 2002), MORB-like mantle ($^3He/^4He$ = 8 ± 1 Ra; Sarda et al., 1988; Ballentine et al., 2002) and atmosphere ($^3He/^4He$ = 1 Ra; Ballentine et al., 2002) make helium the most sensitive proxy for the determination of the sources of the fluids trapped during mineralization and allow to illustrate possible interactions between these fluids and the country rocks (e.g., Mamyrin and Tolstikyn, 2013). Since Simmons et al. (1986), it is accepted that hydrothermal minerals can preserve mantle-derived ^3He. However, there are evidences that in FI-free quartz crystals He may diffuse from the crystal lattice, especially at progressively higher temperatures (e.g., next to or above 400 °C; Shuster and Farley, 2005). On the other hand, the diffusivity through quartz lattice of ^4He seems indistinguishable from that of ^3He, providing no graphical evidence for the commonly expected inverse square root of the mass diffusion relationship between isotopes. This implies that even in case of a diffusive loss of helium, the $^3He/^4He$ should maintain the original signature. Another indication in support of the conservative behavior of He within FI of quartz crystals of hydrothermal origin comes from the evidence that FI may enhance noble gas retentivity in quartz crystals (Shuster and Farley, 2005). In Fig. 8, our data do not show any graphical evidence of He loss as well as $^3He/^4He$ fractionation (even considering ^3He vs R/Ra; Table 3), suggesting that they can be used to constrain the origin of fluids trapped in Ag- and Au-dominant deposits. We notice that the lowest $^3He/^4He$ are recorded in the most He-rich samples, although there is not a unique trend of decrease of $^3He/^4He$ at increasing $^4He_{corr}$ concentration. This behavior strongly indicates mixing between crustal and magmatic fluids, rather than ingrowths of ^4He from the radiogenic decay of U and Th.

The $^3He/^4He$ not corrected for air contamination from San Dimas Eocene Ag-dominant and Oligocene Au-dominant FI present values spanning a wide range (0.07–1.19 Ra), which is in partial overlapping among a few samples from the two distinct deposits. When $^3He/^4He$ is plotted versus $^4He/^{20}Ne$ and $^4He/^{40}Ar$ (Fig. 8D, respectively), we deduce that air-saturated groundwater is the main isotopic reservoir. However, there are clear evidences that fluids from both hydrothermal events mix with fluids from other sources (i.e., crustal and magmatic fluids). In particular, FI trapped in the Eocene Ag-dominant hydrothermal deposits originate from a mixing mostly involving atmospheric and crustal fluids, with a slight contribution of mantle or magmatic ^3He (Fig. 8C and 8D). This could imply that during the Eocene Ag-dominant hydrothermal event faults pathways only marginally reached the basement or magmatic reservoir. Instead, FI trapped in part of the Oligocene Au-dominant hydrothermal deposits track a 3-components mixing that involve atmospheric, crustal, and mantle fluids (Fig. 8C and 8D). In fact, during the Oligocene Au-dominant hydrothermal event continental extension had already produced a thinner crust and involved a deeper faults system (Ferrari et al., 2017; Montoya et al., 2019a, 2019b), creating effective pathways for the mantle derived gases (up to 24%, Table 3) to escape and be subsequently trapped in the mineralized veins. This evidence is also supported by the $\delta^{18}O$-δD values of the Au-dominant hydrothermal event, which indicate that ore fluids are partially magmatic-derived.

In order to figure out what could be the source of ^3He excess in Causita, San Antonio, and Arana samples from Oligocene Au-dominant veins, we plot $^4He_{corr}$ concentration versus Rc/Ra (Fig. 8C), excluding in this way any effect due to atmospheric contamination. If we consider a possible crustal term having $^3He/^4He$ = 0.05 Ra and $^4He_{corr}$ $\sim 2{\cdot}10^{-12}$ mol g^{-1}, we could fit Causita, San Antonio, and Arana samples assuming a binary mixing with a possible local magmatic term having $^3He/^4He \sim 3$ Ra and $^4He_{corr} \sim 2{\cdot}10^{-14}$ mol g^{-1}. This term could correspond to a differentiated magmatic source that resided and degassed within the crust at the time of formation of quartz and that under cooling and ageing conditions lowered its original MORB-like $^3He/^4He$ values (Ballentine et al., 2002; Batista Cruz et al., 2019). This hypothesis has not strong constraints, so we cannot exclude that a magmatic body with higher $^3He/^4He$ and lower ^4He concentration could have supplied fluids trapped in quartz samples. We are only proposing an alternative explanation to the direct rise of ^3He-rich fluids from the local mantle.

Compared to other studies, the range of $^3He/^4He$ values measured in San Dimas Eocene and Oligocene hydrothermal events is significantly lower than those of epithermal deposits and magmatic arc environments ($^3He/^4He$: 0.1–10; Manning and Hosftra, 2017). In the specific case of the Oligocene Au dominant LS-epithermal event, the most comparable with similar deposits, the low $^3He/^4He$ ratios values could be explained by several reasons: (1) analyzed samples do not represent the highest Au grade areas, (2) quartz could present post-entrapment He ingrowth or exchange with external fluids rich in radiogenic ^4He (Kendrick and Burnard, 2011), and (3) despite our attempt to remove secondary inclusions a variable proportion of secondary inclusions probably contributed to enrich FI in the crustal component, saturating the isotopic ratio end member.

In hydrothermal systems, gold and silver transport and deposition depend on fluid composition, temperature, pressure, pH, oxygen and sulphur fugacity, and type and amount of dissolved sulphur and other species (e.g. Mikucki, 1998). The low salinity, low to intermediate sulphidation and near-neutral pH environments and occurrences of several sulphides and sulphosalts, gold–silver from both hydrothermal mineralizing fluids (Tmi = −1.9 to 5.6 °C) pleads in favor of silver and gold transport as $AgHS^-$ and $Au(HS)_2$ complex (Zotov et al.,1995; Barnes, 1997; Cooke and Simmons, 2000; Stefansson and Seward, 2003, 2004; Pokrovski et al., 2014). The stability of $Au(HS)_2$ complexes is greatly increased by the presence of low concentrations of chlorine (Zajacz et al., 2010). Near neutral to slightly alkaline solutions originating in the field of maximum gold solubility as a bisulphide complex produced sericite as the most common potassium aluminosilicate in the alteration assemblages (Romberger, 1986). In the San Dimas district, the Au-dominant vein and telescoped structures are characterized by a well-defined sericite alteration halo, while Eocene Ag-dominant hydrothermal structures are characterized by quartz-adularia-rhodochrosite gangue and chlorite alteration halo (Montoya et al., 2019b). Solubility of $AgHS^-$ and $Au(HS)_2$ is extremely sensitive to changes in temperature and pressure. Depressurization (which occurs during hydraulic fracturing, boiling or as hot fluids ascend up faults) and/or rapid cooling (50 °C or more) decrease Au-Ag solubility by 90% (Zhu et al., 2011). The adiabatic decrease in homogenization temperature recorded in both events and the boiling process observed in Eocene and Oligocene events provided favorable conditions for the deposition of precious metals deposition.

In absence of external geothermometer, pressure and temperature (P-T) trapping conditions could not be estimated for both mineralizing hydrothermal events. However, the chronology of the magmatism and hydrothermal events give us some key information to estimate mineralization depth formation within a reliable geological evolution scenario. The space–time association of Oligocene rhyolitic magmatism with the Au mineralized veins, as well as the chemical and isotopic evidences for a meteoric fluids source (Montoya et al., 2019b), clearly indicate a connection to an air saturated groundwater under hydrostatic P-T conditions. The sericite alteration halos of Au-dominant veins are observed in the stratigraphic column up to the Las Palmas sedimentary formation and are sealed by the Oligocene ignimbrite flows, suggesting that the mineralization structure almost reach the paleosurface, and probably developed within 1 km depth.

The synchronism of Eocene porphyric dikes and Ag mineralized veins, and the chemical evidences for a meteoric fluids source indicate a connection to an air saturated groundwater and degassing process

under hydrostatic P-T conditions, apparently in a shallow position.

However, several authors report that fluids exist at deeper depth in magmatic arcs context (down to 10 km, Menzies et al., 2014 among other). Reliable mineral (chlorite) or isotopic equilibrium geothermometers are needed to correct the minimum fluid inclusion homogenization determination (up to 20 bars). In our case, the alteration induced by the later Oligocene hydrothermal event does not allow to obtain reliable data, but the local geological evolution is well constrained and give us some reliable information. The Piaxla batholith mineral texture and its stratigraphic position, locally overlain by the Camichin sedimentary formation or by the Oligocene ignimbrite flows (~30 Ma, Montoya et al., 2019a), highlight an important extensional tectonic context since the Eocene. Continental conglomerates of Eocene to Oligocene age are widespread in all Central Mexico (Montoya et al., 2019a; Nieto-Samaniego, et al., 2019). At regional scale, the extensional tectonic and exhumation-erosion rate has been estimated at ca. ~0.3 mm/yr (Nieto-Samaniego, et al., 2019), in well agreement with the value for magmatic arc environments (Burkan et al., 2002). Taking into account these observations the difference in the maximum depth formation needed to overlap the Eocene and the Oligocene "bonanza" levels could be estimated at 2–3 km. Such conditions are in agreement to those reported in literature for comparable plutonic related vein deposits (Prokofiev and Pek, 2015; Nieva et al., 2019). At this depth, the silver mineralization trapping temperature, corrected for the hydrostatic pressure, could be estimated at ~350 °C (Steele-MacInnis et al., 2012).

5.2. A new genetic model for the San Dimas district

The San Dimas Ag–Au district is an example of a Eocene-Oligocene telescoped deposit that comprises two mineralizing events: (a) an Eocene Ag-dominant epithermal event (40–41 Ma; Montoya et al., 2019b) associated with the late stage intrusion of a batholith dated at 45–43 Ma (Henry et al., 2003; Montoya et al., 2019a); (b) an Oligocene Au-dominant low sulfidation epithermal event (ca. 30 Ma), associated with rhyolitic volcanism dated at 31–29 Ma (Montoya et al., 2019b). Zircon chemistry also illustrates the most likely magmatic sources for the hydrothermal pulses and thus brackets the age of the mineralization events (Montoya et al., 2019b).

The integration of microthermometry and noble gases, oxygen and deuterium isotope data, in conjunction with a detailed geological re-evaluation and tectonic and petrographic studies, permit a coherent genetic model to be drafted. This model is summarized in Fig. 9.

Eocene silver bearing veins are hosted in the Cretaceous to Paleocene Laramide arc volcanic sequence (Lower Volcanic Complex). Ag-dominant mineralization structures are mainly hosted in E-W sigmoidal gashes and geographically distributed in proximity with the Eocene Piaxtla batholith (Montoya et al., 2019a). The Ag-dominant veins are composed of different quartz and breccia events and are characterized by adularia and rhodochrosite gangue. The proximity of the epithermal alteration $^{40}Ar/^{39}Ar$ cooling ages (41–40 Ma) and the U/Pb zircon ages of the Piaxla batholith last magmatic pulses (45–43 Ma) support a genetic relationship (Montoya et al., 2019a, b). The continuous enrichment of the Eu/Eu* and (Ce/Nd)/Y) ratios through time, from 50 to 43 Ma in zircon crystals, strongly suggest that the most enriched magmatism occurred during the last and shallowest stage of the batholith formation (Montoya et al., 2019b). It is reasonable to suppose that the batholith building process not only provided the heat, part of the fluids and the metals, but also generated shallow extension and the formation of mineralized tension gashes during its ascent. The Piaxla batholith shallow position in the stratigraphic column suggest the enrichment of the magma in precious metals and metalloids by assimilation of the Cretaceous porphyry bodies (Montoya et al., 2019a), as recognized in other granite-related deposits in Northwest Europe (Nieva et al., 2019; Vallance et al., 2003). Furthermore, during the batholith emplacement the thermal anomaly remained elevated for a long period of time. In such geological environment, the mineralized fluids could come from three reservoirs: magmatic, metamorphic and/or meteoric. Microthermometry results, O-D, H_2O and CO_2 concentration, as well as noble gases trapped in FI, all point to the dominance of meteoric fluid, or air saturated groundwater in the hydrothermal system. He isotopes indicate that magmatic/mantle fluids are very low to negligible (< 2%), with a dominant contribution by a crustal reservoir, in good agreement with the geological context. The low salinity of the fluids (Tmi = −1.9 to 5.6 °C; wt% NaCl eq = 0–3.22 wt%) pleads in favor of silver transport as a bisulphur complex ($AgHS^-$; Zotov et al., 1995; Barnes, 1997). Hydrosulphide complex is dominant in neutral to alkaline pH and moderate to low salinity fluid (Akinfiev and Zotov, 2001; Gammons and Barnes, 1989; Seward and Barnes, 1997). In this situation, degassing may be more effective for silver deposition rather than conductive cooling or mixing. According to Stefansson and Seward, (2003), the hydrosulphide complex of silver can be stable in a wide range of temperature so that mixing or cooling may not dramatically reduce its solubility. However, the gas separation during degassing leads to the loss of volatile H_2S, which can effectively break the hydrosulphide complex and cause the deposition of silver (Seward, 1989; Stefansson and Seward, 2003). During the filling stage, hydraulic breccia and the evidence of heterogeneous trapping of FI illustrate the boiling/degassing process. Silver precipitation was probably linked to cooling temperature and pressure drop/boiling during the batholith ascent (Vallance et al., 2003).

The Eocene Ag-dominant mineralization event does not fit into a classic metallogenetic model. Based on the mineral paragenesis and following the literature of Mexican deposits it would be classified as intermediate sulphidation silver epithermal deposit (Camprubí and Albinson, 1996). In fact, these deposits are commonly hosted in calc-alkaline andesitic-dacitic arcs and found at the margins of high-sulphidation and/or porphyry deposits (John, 1999; 2001). The historical classification of San Dimas district as an IS epithermal deposit was based on mineralogical paragenesis and an incomplete knowledge of the chronological and geological context (Enriquez et al., 2018; Montoya et al., 2019b). If we accept the intermediate sulphidation character of the San Dimas Ag mineralization, the epithermal concept does not seem the better representation for such a deep (2–3 km), high temperature (up to ~350 °C) and plutonic-related deposit. However, the Eocene Ag-dominant mineralization event has also several characteristics that do not fit into the traditional "intrusion-related" type (IRGS; Lang and Baker, 2001; Hart, 2005), such as the location above a large and elongated batholith, the absence of regional mineralogical zonation with As–Au at the center of the batholith and Ag–Pb–Zn associations at the periphery, the very low gold content, a low sulphur fugacity and the dominant meteoric fluids.

The Oligocene Au-dominant mineralization structures are mainly hosted in N-S faults systems that have undergone multiple reactivations and are geographically and chronologically associated with Oligocene rhyolitic domes (at ca. 30 Ma, Montoya et al., 2019b). The Au-dominant veins are characterized by a single hydrothermal pulse, an intense sericitization and low-temperature formation (FI homogenization temperatures of 121 °C to 316 °C). The Au, Hg, Sb, and Bi metals association is commonly related to shallow epithermal systems (Gray et al.,1991; Bornhorst et al., 1995). The source of the fluids in this model, like classic LS epithermal models (Henley, 1986; Sillitoe, 1993; Hedenquist et al., 2000), is meteoric. The low salinity of the fluids (Tmi = −1.4 to 0.0 °C; wt% NaCl eq = 0–2.40 w%) argues in favor of gold transport as a bisulfide complex ($AuHS_2^-$; Zotov et al., 1995; Barnes, 1997). The paragenetic mineralogy, the low salinity of the fluids, as well as their gas content (H_2O > 99.5 mol percent of the liquid and gas phases, with CO_2 comprising most of the remaining gases, minor CO and traces of H_2, CH_4, N_2, C_2H_6, H_2S, C_3H_8, SO_2 and NO; Smith et al., 1982), is characteristic of the low sulphidation epithermal type (Henley, 1986). Concerning the sources of the FI trapped in quartz, H_2O reveals the dominant species as in Ag-dominant deposits. Ar-Ne-He isotopic

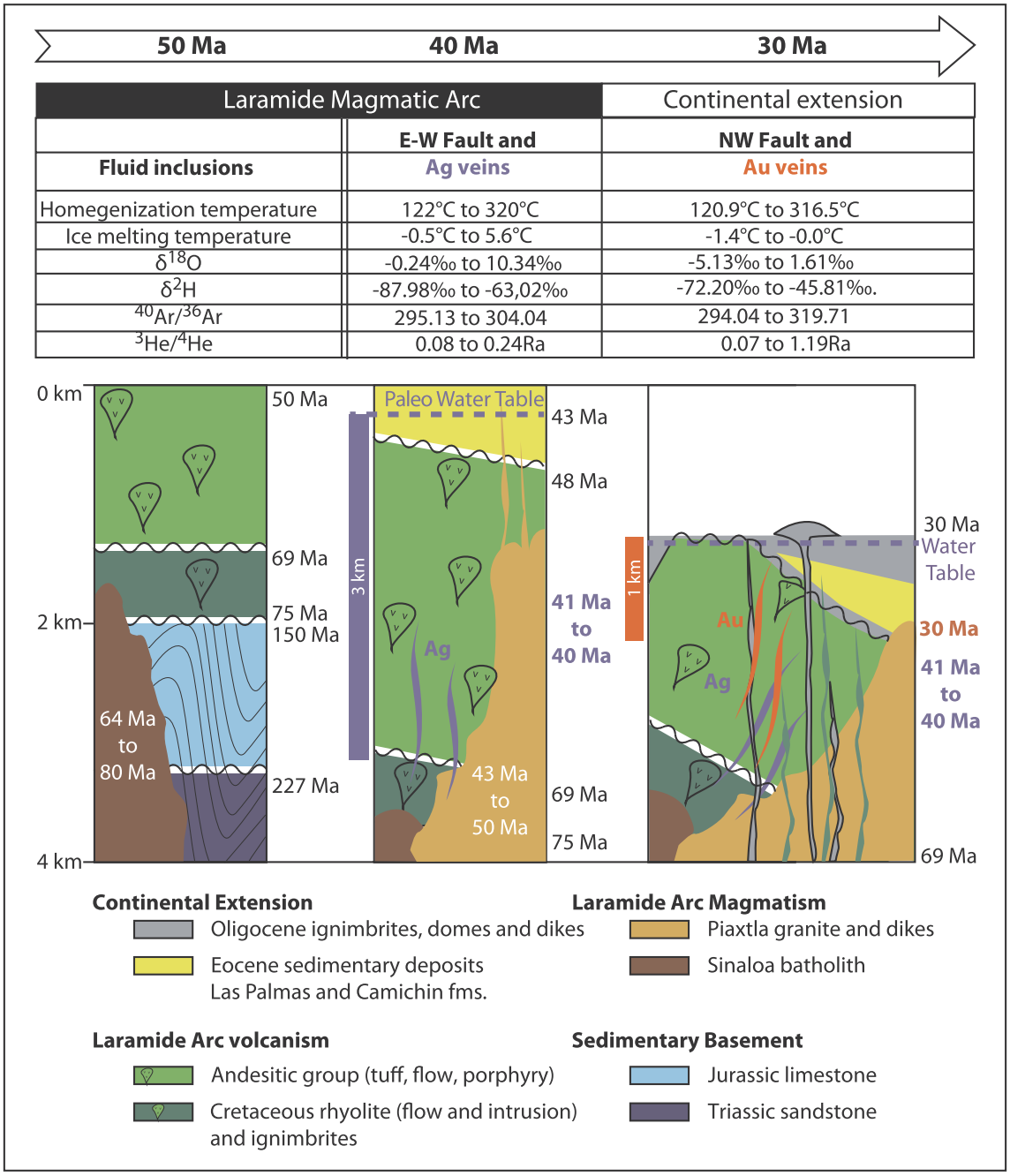

Fig. 9. Genetic model for the evolution for the Eocene-Oligocene telescoped San Dimas Ag–Au deposit. Boxes summarize the isotopic characteristics of the different reservoirs. Helium isotopic results are given in $^{3}He/^{4}He$ (Rac) ratios, and oxygen and deuterium in ‰ deviation relative to the SMOW standard. The synthesized geological cross-section is drawn from the East-West transect (modified from Montoya et al., 2019b). For legend, see Fig. 2.

systematics illustrates a hydrothermal system dominated by air saturated groundwater. Helium isotopes indicate that a not negligible contribution to FI has a magmatic/mantle origin (up to 24%), although some samples show a classical crustal signature. The Oligocene Au-dominant mineralization event matches all the geological and geochemical characteristics of the gold low sulphidation epithermal deposit model (Henley, 1986; Campbell and Larson, 1998).

As a consequence, it seems likely that the development of the San Dimas Oligocene Au-dominant mineralization event and probably many other epithermal precious metal deposits are related to the activation of extensional or transtensional fault systems within a major crustal discontinuity rooted in the lower crust or even in the mantle. The ascent of bimodal magma batches is accompanied by fluids rich in gas and sulphur, promoting the gold transport. The reactivation of the NNW-SSE structural corridor at ca. 30 Ma was an important event in the evolution of the SMO during a major pulse of crustal thinning associated to the ascent of asthenospheric melts (Ferrari et al., 2017). This process was accompanied by the melting of the mantle lithosphere and the lower crust and could explain the temporal and spatial association between the ascent of deep mineralizing fluids and silicic magmatism, and upper crustal extensional structures.

Finally, our study highlights the necessity to integrate geological observations and independent chronological and geochemical techniques to better understand the complexity of the hydrothermal magmatic processes involved in the formation of many Mexican ore deposits.

Declaration of Competing Interest

The authors declare that they have no known competing financial interests or personal relationships that could have appeared to influence the work reported in this paper.

Acknowledgments

This research is part of the PhD project of the first author at Universidad Nacional Autónoma de Mexico (UNAM) Postgraduate Program. The research was funded by CONACYT grant CB-237745-T and PAPIIT IV100117 to L. Ferrari. We thank Primero Mining (presently First Majestic Silver Corp.) for sharing unpublished information and for logistical support. Special thanks to Nicolas Landón for his strong support in the initial phase of the research and to Miguel Pérez for sharing his knowledge or the ore geology on the central SMO. We also thank Marina Vega for assistance at Laboratorio de Fluidos Corticales, personnel at Stable Isotope Laboratory at Laboratorio Nacional de Geoquímica y Mineralogía, Instituto de Geología, Universidad Nacional Autónoma de México, Ciudad de México, and Juan Tomás Vazquez for the elaboration of thin sections. We thank Maria Grazia Misseri and Mariano Tantillo from INGV-Palermo for helping in samples preparation, H2O-CO2 concentration, and noble gases isotope analysis of fluid inclusions, as well as Fausto Grassa for useful discussions on data elaboration. Authors are special grateful to Seequent for providing an academic license of Leapfrog Mining.

Appendix A. Supplementary data

Supplementary data to this article can be found online at https://doi.org/10.1016/j.oregeorev.2020.103427.

References

Akinfiev, N., Zotov, A., 2001. Thermodynamic description of chloride, hydrosulfide, and hydroxo complexes of Ag (I), Cu (I), and Au (I) at temperatures of 25–500°C and pressures of 1–2000 bar. Geochem. Int. 39, 990–1006.

Albinson, T., Norman, D.I., Cole, D., Chomiak, B., 2001. Controls on formation of low sulfidation epithermal deposits in Mexico: Constraints from fluid inclusion and stable isotope data. In: New Mines and Discoveries in Mexico and Central America. Society of Economic Geology Special Publication, 8, 1–32.

Ballentine, C.J., 1997. Resolving the mantle He/Ne and crustal 21Ne/ 22Ne in well gases. Earth Planet. Sci. Lett. 152, 233–249.

Ballentine, C.J., Mazurek, M., Gautschi, A., 1994. Thermal constraints on crustal rare gas release and migration: Evidence from Alpine fluid inclusions. Geochim. Cosmochim. Acta 58, 4333–4348.

Ballentine, C., Burgess, R., Marty, B., 2002. Tracing fluid origin, transport and interaction in the crust. In: Porcelli, D., Ballentine, C.J., Wieler, R. (Eds.), Noble Gases. Geochemistry and Cosmochemistry, 47, 539–614.

Barnes, H., 1997. Geochemistry of Hydrothermal Ore Deposits, Third Edition. Wiley-Interscience Inc., New York.

Batista Cruz, R.Y., Rizzo, A.L., Grassa, F., Bernard Romero, R., González Fernández, A., Kretzschmar, T.G., Gómez-Arias, E., 2019. Mantle degassing through continental crust triggered by active faults: The case of the Baja California Peninsula, Mexico. Geochem. Geophys. Geosyst. 20, 1912–1936.

Bodnar, R., Reynolds, T., Kuehn, C., 1985. Fluid inclusion systematics in epithermal systems, In: Berger, B.R., Bethke, P.M. (Eds.), Geology and geochemistry of epithermal systems. Rev. Economic Geology, 2, 73–97.

Bornhorst, T., Nurmi, P., Rasilainen, K., Kontas, E., 1995. Trace element characteristics of selected epithermal gold deposits of North America. Geol. Surv. Finland Spec. Pap. 20, 47–52.

Burlinson, K., 1988. An instrument for fluid inclusion decrepitometry and examples of its application. Bull. Mineral. 111, 267–278.

Burlinson, K., Dubessy, J., Hladky, G., Wilkins, R., 1983. The use of fluid inclusio decrepitometry to distinguish mineralised and barren quartz veins in the Aberfoyle tin-tungsten mine area. J. Geochem. Explor. 19, 319–333.

Campbell, A., Larson, P., 1998. Introduction to stable isotope applications in hydrothermal systems. Rev. Econ. Geol. 10, 173–193.

Camprubí, A., 2013. Tectonic and Metallogenic History of Mexico. Soc. Econ. Geol., Special Publication 17, 201–243.

Camprubí, A., Albinson, T., 1996. Depósitos epitermales en México: Actualización de su conocimiento y reclasificación empírica. Boletín de la Sociedad Geológica Mexicana 58, 27–81.

Camprubí, A., Albinson, T., 2007. Epithermal deposits in México-Update of current knowledge, and an empirical reclassification. Geol. Soc. Am. Special Papers 422 (14), 377–415.

Chen, Y., Bao, J., Zhang, Z., Chen, H., Liu, Y., 2003. Laumontitization as exploration indicator of epithermal gold deposits: A case study of the Axi and other epithermal systems in West Tianshan, China. Geochem. J. 22, 289–303.

Chen, Y., Pirajno, F., Wu, G., Qi, J., Xiong, X., 2012. Epithermal deposits in North Xinjiang, NW China. Int. J. Earth Sci. 101, 889–917.

Churchill, R.K., 1980. Meteoric water leaching and ore genesis at the Tayoltita silver-gold mine, Durango, Mexico. Unpublished Ph.D. dissertation, 162.

Clarke, M., Titley, S., 1988. Hydrothermal evolution in the formation of silver-gold veins in the Tayoltita mine, San Dimas district, Mexico. Econ. Geol. 83 (8), 1830–1840.

Conrad, M., Chamberlain, C.P., 1992. Laser-based, in situ measurements of fine-scale ariations in the $\partial^{18}O$ of hydrothermal quartz. Geology 20 (9), 812–816.

Cooke, D., Simmons, S., 2000. Characteristics and genesis of epithermal gold deposits – SEG Reviews. Econ. Geol. 13, 221–244.

Einaudi, M., 1992. Ore deposits in the Oquirrh and Wasatch Mountains, Utah: Examples of large-scale water-rock interaction. In: eds,, . (Ed.), Kharaka and Maest. Water-Rock Interaction, pp. 879–887.

Enriquez, E., Rivera, R., 2001. Geology of the Santa Rita Ag-Au Deposit, San Dimas District, Durango, Mexico. Special Publication, Soc. Econ. Geol. 8, 39–58.

Enríquez, E., Iriondo, A., Camprubí, A., 2018. Geochronology of Mexican mineral deposit. VI: The Tayoltita low-sulfidation epithermal Ag-Au district, Durango and Sinaloa. Boletín de la Sociedad Geológica Mexicana 70 (2), 531–547.

Ferrari, L., Valencia-Moreno, M., Bryan, S., 2007. Geology of the western Mexican volcanic belt and adjacent Sierra Madre Occidental and Jalisco block, in Delgado-Granados. Geol. Soc. Am. Spec. Pap. 334, 65–83.

Ferrari, L., López-Martínez, M., Orozco-Esquivel, T., Bryan, S., Duque-Trujillo, J., Lonsdale, P., 2013. Late Oligocene to Middle Miocene rifting and synextensional magmatism in the southwestern Sierra Madre Occidental, México: The beginning of the Gulf of California rift. Geol. Soc. Am. 9 (5), 1–40.

Ferrari, L., Orozco, T., Bryan, S., Lopez, M., Silva, A., 2018. Cenozoic extension and magmatism in western Mexico: Linking the Sierra Madre Occidental Silicic Large Igneous Province and the Comondú Group with the Gulf of California rift. Earth-Sci. Rev. 183, 115–152.

Gammons, C., Barnes, H., 1989. The solubility of Ag2S in near-neutral aqueous sulfide solutions at 25 to 300°C. Geochim. Cosmochim. Acta 53, 279–290.

Giggenbach, W., 1992a. Magma degassing and mineral deposition in hydrothermal systems along convergent plate boundaries. Econ. Geol. 87, 1927–1944.

Giggenbach, W.F., 1992b. The composition of gases in geothermal and volcanic systems as a function of tectonic setting. International Symposium Water-Rock Interaction 7th, Park City, 873–878.

Graham, D.W., 2002. Noble gas isotope geochemistry of Mid-Ocean ridge and Ocean island basalts: Characterization of mantle source reservoirs. In Noble Gases in Geochemistry and Cosmochemistry, Rev. Mineral. Geochem. 47, In: Porcelli, D.P., Ballentine, C.J., Wieler, R. (Eds.), Mineralogical Society of America, 247–317.

Gray, D., Goldfarb, R., Detra, D., Slaughter, K., 1991. Geochemistry and exploration criteria for epithermal cinnabar and stibnite vein deposits in the Kuskokwim River region, southwestern Alaska. J. Geochem. Explor. 41, 363–386.

Hart, C., 2005. Classifying, distinguishing and exploring for intrusion-related gold systems: The Gangue. Newslett. Geol. Assoc. Can. Miner. Deposits Div. 87, 4–9.

Heald, P., Foley, N., Hayba, D., 1987. Comparative anatomy of volcanic-hosted epithermal deposits: Acid-sulfate and adularia-sericite types. Econ. Geol. 82 (1), 1–26.

Hedenquist, J.W., 1987. Mineralization associated with volcanic-related hydrothermal systems in the circum-Pacific basin: Circum Pacific. Energy and Mineral Resource Conference, 4th, Singapore, August 17–22, 513–524.

Hedenquist, J.W., Arribas, A.J., 2000. Epithermal gold deposits: I. Hydrothermal processes in intrusion-related systems, and II. Characteristics, examples and origin of epithermal gold deposits. Soc. Econ. Geol. 31, 13–63.

Henley, R.W., Hedenquist, J.W., 1986. Introduction to the geochemistry of active and fossil geothermal systems. In: Henley, R.W., Hedenquist, J.W., Roberts, P.J. (Eds.), Guide to the active epithermal systems and precious metal deposits of New Zealand. Monography Series Mineral Deposits, 26, 129–145.

Henry, C., McDowell, F., Silver, L., 2003. Geology and geochronology of granitic batholithic complex, Sinaloa, México: Implications for Cordilleran magmatism and tectonics. Geological Society of America, Special Paper 374: Tectonic evolution of northwestern Mexico and the Southwestern USA, Vol. 374, pp. 237–273.

Henry, D., Fredrikson, G., 1987. Geology of southern Sinaloa adjacent to the Gulf of California. Geological Society of America, Map and Chart Series. Map MCH063, 14p.

Henshaw, P.C., 1953. Geology and Ore Deposit of the San Dimas District. Sinaloa and Durango, Private document, pp. 531.

Horner, J., Enriquez, E., 1999. Epithermal precious metal mineralization in a strike-slip corridor: The San Dimas District, Durango, Mexico. Econ. Geol. 94 (8), 1375–1380.

John, D., 1999. Magmatic influence on characteristics of Miocene low-sulfidation Au-Ag deposits in the northern Great Basin (abs). Geol. Soc. Am. Abstracts Program 31 (7), pp. A-405.

John, D.A., Garside, L.J., Wallace, A.R., 1999. Magmatic and tectonic setting of late Cenozoic epithermal gold-silver deposits in northern Nevada, with an emphasis on the Pah Rah and Virginia Ranges and the northern Nevada rift: Geological Society of Nevada. Spring Field Trip Guidebook Special Publication 29, 64–158.

John, D., 2001. Miocene and Pliocene epithermal gold-silver deposits in the northern Great Basin, western USA: Characteristics, distribution, and relationship to magmatism. Econ. Geol. 96, 1827–1853.

Kendrick, M., Burnard, P., 2011. Noble gases and halogens in fluid inclusions: a journey through the earth's crust. In: The noble gases as geochemical tracers. Springer, Berlin, Heidelberg, pp. 319–369.

Kennedy, B.M., Hiyagon, H., Reynolds, J.H., 1990. Crustal neon: A striking uniformity. Earth Planetary Sci. Lett. 98, 277–286.

Kerrich, R., Goldfarb, R., Groves, D., Garwin, S., Jia, Y., 2000. The characteristics, origins, and geodynamic settings of supergiant gold metallogenic provinces. Sci. China (Series D) 43, 68.
Lang, J., Baker, T., 2001. Intrusion-related gold systems: The present level of understanding. Miner. Deposita 36, 477–489.
Leach, T., Corbett, G., 1994. Porphyry-related carbonate-base-metal gold systems: Characteristics. In: Rogerson, R. (Ed.), Geology, exploration and mining conferences. The Australasian Institute of Mining and Metallurgy, 84–91.
Lindgren, W., 1922. A suggestion for the terminology of certain mineral deposits. Econ. Geol. 17 (4), 292–294.
Lindgren, W., 1933. Mineral deposits. McGraw-Hill Book Company Inc, London.
Mamyrin, B., Tolstikyn, I., 2013. Helium isotope in nature. Dev. Geochem. 3, 273p.
Manning, A.H., Hostra, A.H., 2017. Noble gas data from Goldfield and Tonopah epithermal Au-Ag deposits, ancestral Cascades Arc, USA: Evidence for a primitive mantle volatile source. Ore Geol. Rev. 89, 683–700.
Mikucki, E., 1998. Hydrothermal transport and depositional processes in Archean lode-gold systems: A review. Ore Geol. Rev. 13, 307–321.
Moncada, D., Baker, D., Bodnar, R., 2017. Mineralogical, petrographic and fluid inclusion evidence for the link between boiling and epithermal Ag-Au mineralization in the La Luz area, Guanajuato Mining District, México. Ore Geol. Rev. 89, 143–170.
Moncada, D., Mutchler, S., Nieto, A., Reynolds, T.J., Rimistidt, J.D., Bodnar, R.J., 2012. Mineral textures and fluid inclusion petrography of the epithermal Ag-Au deposits at Guanajuato, Mexico: Application to exploration. J. Geochem. Explor. 114, 20–35.
Montoya-Lopera, P., Ferrari, L., Levresse, G., Abdullin, F., Mata, L., 2019a. New insights into the geology and tectonics of the San Dimas mining district, Sierra Madre Occidental, Mexico. Ore Geol. Rev. 105, 273–294.
Montoya-Lopera, P., Levresse, G., Ferrari, L., Orozco-Esquivel, T., Hernandez-Quevedo, G., Abdullin, F., 2019b. New geological, geochronological and geochemical characterization of the San Dimas mineral system: Evidence for a telescoped Eocene-Oligocene Ag/Au deposit in the Sierra Madre Occidental, Mexico. Ore Geology Reviews. In press.
Nieto-Samaniego, A., Olmos-Moya, M., Levresse, G., Alaniz-Alvarez, A., Abdullin, F., Pilar-Martinez, A., 2019. Thermochronology and exhumation rates of granitic intrusions at Mesa Central, Mexico. Int. Geol. Rev. 1–8.
Nieva, A.M.R., Moura, A., Leal gomes, C.A., Pereira, M.F., Corfu, F.,, 2019. The granite-hosted Variscan gold deposit from Santo Antonio mine in the Iberian massif (penedono, NW Portugal): Constraints from mineral chemistry, fluid inclusions, sulfur and noble gases isotopes. J. Iberian Geol. 1–27.
Ozima, M., Podosek, A.P., 2002. Noble Gas Geochemistry, second, ed. Cambridge University Press, Cambridge, pp. 10–15.
Panteleyev, A., 1996. Epithermal Au-Ag: Low sulphidation, in selected British Columbia Mineral Deposit Profiles. British Columbia Ministry of Employment and Investment, Open File 2, 41–44.
Pinti, D.L., Castro, M.C., Shouakar-Stash, O., Tremblay, A., Garduño, V.H., Hall, C.M., Helie, J.F., Ghaleb, B., 2013. Evolution of the geothermal fluids at Los Azufres, Mexico as traced by noble gases ∂18O, ∂D, ^{13}C and $^{87}Sr/^{86}Sr$. J. Volcanol. Geoth. Res. 249, 1–11.
Pirajno, F., 2009. Hydrothermal processes and mineral systems. Springer, Berlin, Australia, pp. 1250p.
Pokrovski, Gleb S., Akinfiev, Nikolay N., Borisova, Anastassia Y., Zotov, Alexandre V., Kouzmanov, Kalin, 2014. Gold speciation and transport in geological fluids: Insights from experiments and physical-chemical modelling. Geological Society, London, Special Publications 402 (1), 9–70. https://doi.org/10.1144/SP402.4.
Prokofiev, V., Pek, A., 2015. Problems in estimation of the formation depth of hydrothermal deposits by data on pressure of mineralization fluids. Geol. Ore Deposits 57, 1–20.
Ramos-Rosique, A., Bryan, S., Ferrari, L., Allen, C., Lopez-Martinez, M., Rankin, A., 2010. Timing and evolution of Late Oligocene to Miocene magmatism in the southern Sierra Madre Occidental silicic large igneous province: Insights from zircon chronochemistry and $^{40}Ar/^{39}Ar$ geochronology. EGU General Assembly Conference Abstracts 12, 9788.
Romberger, S., 1986. Ore deposits #9 Disseminated gold deposits. Geosci. Can. 13, 23–31.
Sarda, P., Staudacher, T., Allegre, C.J., 1988. Neon isotopes in submarine basalts. Earth Planetary Sci. Lett. 91, 73–88.
Seward, T., 1989. The hydrothermal chemistry of gold and its implications for ore formation: Boiling and conductive cooling as examples. Econ. Geol. Monogr. 6, 398–404.
Seward, T., Barnes, H., 1997. Metal transport by hydrothermal ore fluids. In: Dans H.. Barnes, Geochemistry of hydrothermal ore deposits, (third ed.) John Wiley and Sons, New York, 435–486.
Sheppard, S., 1986. Characterization and isotopic variations in natural waters. In: Valley, J.W., Taylor, H.P.J., O'Neil, J.R., (Eds)., Stable isotope in high temperature geological processes. Mineralogical Society of America, Reviews in Mineralogy, 16, 165–183.
Sheppard, S., Nielsen, R., Taylor, H., 1969. Oxygen and hydrogen isotope ratios of clay minerals from porphyry copper deposits. Econ. Geol. 64, 755–777.
Shuster, D.L., Farley, K.A., 2005. Diffusion kinetics of proton-induced ^{21}Ne, ^{3}He, and ^{4}He in quartz. Geochim. Cosmochim. Acta 69, 2349–2359.
Simmons, S.F., White, N.C., John, D.A., 2005. Geological characteristics of epithermal precious and base metal deposits. Society of Economic Geologist, 100th Anniversary, 485–522.
Simmons, S., Sawkins, F., Schlutter, D., 1986. Mantle derived helium in two hydrothermal ore deposits, Peru. Nature 329, 429–432.
Smith, D., Albinson, T., Sawkins, F., 1982. Geologic and fluid inclusion studies of the Tayoltita silver-gold vein deposit, Durango Mexico. Soc. Econ. Geol. 1120–1145.
Steele-Maclnnis, M., Lecumberri-Sanchez, P., Bodnar, R., 2012. Short note: HokieFlincs_H_2O-NaCl: A Microsoft Excel spreadsheet for interpreting microthermometric data from fluid inclusions based on the PVTX properties of H_2O-NaCl. Comput. Geosci. 49, 334–337.
Stefansson, A., Seward, T., 2003. Experimental determination of the stability and stoichiometry of sulphide complexes of silver (I) in hydrothermal solutions to 400°C. Geochim. Cosmochim. Acta 67, 1395–1413.
Stefansson, A., Seward, T., 2004. Gold (I) complexing in aqueous sulphide solutions to 500°C at 500 bars. Geochemica et Cosmochimica Acta 68 (20), 4121–4143.
Taylor, H., 1974. The application of oxygen and hydrogen isotopic studies to problems of hydrothermal alteration and ore deposition. Econ. Geol. 69 (6), 843–883.
Vallance, J., Cathelineau, M., Boiron, M., Fourcade, S., Shepherd, T., Naden, J., 2003. Fluid-rock interactions and the role of late Hercynian aplite intrusion in the genesis of the Castromil gold deposit, northern Portugal. Chem. Geol. 194, 201–224.
Velador, J., Heizler, W., Campbell, A., 2010. Timing of magmatic activity and mineralization and evidence of a long-lived hydrothermal system in the Fresnillo silver district, Mexico: Constraints from $^{40}Ar/^{39}Ar$ geochronology. Econ. Geol. 105, 1335–1349.
Wang, J., Wang, X., Liu, J., Zhai, D., Wang, Y., 2019. Geology, geochemistry, and geochronology of gabbro from the Haoyaoerhudong Gold Deposit, Northern Margin of the North China Craton. Minerals 9, 63.
White, C., 2003. Epithermal Gold Deposits. Society of Economic Geologist Beijing Gold Workshop 25–26 Oct, 118.
Zajacz, Z., Seo, J., Candela, P., Piccoli, P., Heinrich, C., Guillong, M., 2010. Alkali metals control the release of gold from volatile-rich magmas. Earth Planet. Sci. Lett. 297, 50–56.
Zamora-Vega, O., Richards, J., Spell, T., Dufrane, S., Williamson, J., 2018. Multiple mineralization events in the Zacatecas Ag-Pb-Zn-Cu-Au district, and their relationship to the tectonomagmatic evolution of the Mesa Central, Mexico. Ore Geol. Rev. 102, 519–561.
Zhang, C., Wang, E., Bi, Z., Han, R., Shao, J., Liu, B., 2019. Geochronology and isotope geochemistry studies of an epithermal gold deposit in the northern Lesser Khingan Range, NE China: The Gaosongshan example. Ore Geol. Rev. 105, 356–374.
Zhu, Y., An, F., Tan, J., 2011. Geochemistry of hydrothermal gold deposits: A review. Geosci. Front. 2 (3), 367–374.
Zotov, A., Kudrin, A., Levin, K., Shikina, N., VaŕYash, L., 1995. Experimental studies of the solubility and complexing of selected ore elements (Au, Ag, cu, Mo, As, Sb, Hg) in aqueous solutions. In: Shmulovich, K.L., Yardley, B.W.D., Gonchar, G.G. (Eds.), Fluids in the Crust. Equilibrium and Transport Properties, 95–138.